

Precision Determination of Atmospheric Extinction at Optical and Near IR Wavelengths

David L. Burke¹, T. Axelrod², Stéphane Blondin^{3,4}, Chuck Claver⁵, Željko Ivezić⁶,
Lynne Jones⁶, Abhijit Saha⁵, Allyn Smith⁷, R. Chris Smith⁸, Christopher W. Stubbs⁹

¹SLAC National Accelerator Laboratory, Menlo Park, CA, 94025 USA

²Steward Observatory, University of Arizona, Tucson, AZ, 85718 USA

³ESO, Karl-Schwarzschild-Str. 2 85748 Garching, Germany

⁴CPPM, CNRS-IN2P3, 13288 Marseille cedex 09, France

⁵National Optical Astronomy Observatory, Tucson, AZ, 85718 USA

⁶Department of Astronomy, University of Washington, Seattle, WA, 98195, USA

⁷Department of Physics and Astronomy, Austin Peay State University, Clarksville, TN,
37044 USA

⁸Cerro Tololo Inter-American Observatory, Casilla 603, La Serena, Chile

⁹Harvard Smithsonian Center for Astrophysics, Harvard University, Cambridge, MA, 02138
USA

daveb@slac.stanford.edu

Received _____; accepted _____

ABSTRACT

The science goals for future ground-based all-sky surveys, such as the Dark Energy Survey, PanSTARRS, and the Large Synoptic Survey Telescope, require calibration of broadband photometry that is stable in time and uniform over the sky to precisions of a per cent or better, and absolute calibration of color measurements that are similarly accurate. This performance will need to be achieved with measurements made from multiple images taken over the course of many years, and these surveys will observe in less than ideal conditions. This paper describes a technique to implement a new strategy to directly measure variations of atmospheric transmittance at optical wavelengths and application of these measurements to calibration of ground-based observations. This strategy makes use of measurements of the spectra of a small catalog of bright “probe” stars as they progress across the sky and back-light the atmosphere. The signatures of optical absorption by different atmospheric constituents are recognized in these spectra by their characteristic dependences on wavelength and airmass. State-of-the-art models of atmospheric radiation transport and modern codes are used to accurately compute atmospheric extinction over a wide range of observing conditions. We present results of an observing campaign that demonstrate that correction for extinction due to molecular constituents and aerosols can be done with precisions of a few millimagnitudes with this technique.

Subject headings: atmospheric effects - methods:observational - surveys - techniques:photometric

1. Introduction

A modern astronomical telescope instrumented with a digital camera will count a fraction of the photons produced by a celestial source that reach the electronic detector during an exposure. For ground-based broad-band observations the sum of the digital counts (ADU) associated with a source is proportional to the integral of the optical flux $F_\nu(\lambda)$ from the source that reaches *the top of the atmosphere* weighted by the observational bandpass, $T_b(x, y, alt, az, t, \lambda)$,

$$ADU_b^{meas} = A\Delta T \int_0^\infty F_\nu(\lambda) T_b(x, y, alt, az, t, \lambda) \lambda^{-1} d\lambda, \quad (1)$$

where A is the area of the telescope pupil and ΔT is the duration of the exposure. The units of flux $F_\nu(\lambda)$ are $\text{ergs cm}^{-2} \text{ s}^{-1} \text{ Hz}^{-1}$, and the factor $\lambda^{-1} d\lambda$ counts the number of photons per unit energy at a given wavelength. (Strictly, this should be $(h\lambda)^{-1} d\lambda = -(h\nu)^{-1} d\nu$, but the units can be chosen to absorb the factor of Planck’s constant h into the definition of the instrumental system response.) The coordinates (x, y) are those of the source image in the focal plane of the camera, (alt, az) are the altitude and azimuth of the telescope pointing, and t is the time (and date) of the observation.

Assuming the atmospheric and instrumental properties are uncorrelated, the optical passband can be separated into two functions,

$$T_b(x, y, alt, az, t, \lambda) = T_b^{inst}(x, y, t, \lambda) \times T^{atm}(alt, az, t, \lambda), \quad (2)$$

where T^{atm} is the optical transmittance (dimensionless) from the top of the atmosphere to the input pupil of the telescope, and T_b^{inst} is the instrumental system response (ADU/photon) from photons through the input pupil of the telescope to ADU counts in the camera. The instrumental “throughput” includes the reflectance of the mirrors, transmission of the refractive optics and optical filters, efficiency of the camera sensors, and the gain of the electronics used to read out the detectors.

The instrumental throughput T_b^{inst} is usually measured with some combination of artificial illumination with diffuse light from a reflector screen mounted in the dome of the telescope housing, and sky flats assembled from either exposures of the twilight sky and/or combined stacks of images taken through the night. But dome flats and sky flats are, at best, sources of uniform surface brightness that fill the focal plane, while celestial sources produce localized groups of counts that are aggregated by the image reduction software. The two include differing patterns of stray and scattered light that must be reconciled to create a true instrumental normalization (i.e. “flat field”) for the science exposures. This “illumination” correction is usually determined by taking a series of exposures rastered over a small area of sky, and processing the images to extract counts from individual sources (usually stars) as they are detected on differing parts of the focal plane (Manfroid 1996) (Marshall & DePoy 2005) (Regnault et al. 2009).

Astronomers traditionally, e.g. (Sterken 2006), measure a broad-band atmospheric extinction coefficient K_b by interleaving observations of science targets with observations of standard stars over a range of airmass (z) throughout the observing night. In the simplest analysis, the observed magnitudes are fit to a first-order linear behavior in airmass,

$$m_b = m_b^0 + K_b z. \quad (3)$$

In principle fits can be made to data taken at different times in the night, but frequently only a single nightly coefficient is determined due to limited observing time. But the combination of these measurements with those made of the instrumental response provides a determination of the observational bandpass that can be interpolated to the coordinates (x, y, alt, az, t) of the science observations.

If care is taken to manage effects of thermal changes and systematic effects due to the mechanics of the telescope, then it is possible to obtain a relatively stable instrumental response throughout a night of observing. Careful analysis can reduce errors in the flat

fielding across small fields of view to percent accuracies (Landolt 1992) (Stetson 2005). But the atmospheric transmittance can vary considerably more rapidly and by significantly greater amounts. Precise photometry is traditionally done only during times when atmospheric conditions are stable and clear of clouds. A night is generally regarded as “photometric” if multiple observations of the same target yield sufficiently small variations in measured magnitudes.

1.1. Calibration of All Sky Surveys

The science goals for future ground-based all-sky surveys, such as the Dark Energy Survey (DES) (Flaugher 2007), PanSTARRS (Kaiser et al. 2002), and the Large Synoptic Survey Telescope (LSST) (Ivezic et al. 2009) pose stringent requirements on the stability and uniformity of photometric measurements. These surveys seek relative calibration of photometry that is stable in time and uniform over the sky to precisions of a per cent or better, and absolute calibration of color measurements that are similarly accurate. This performance will need to be achieved with measurements made from multiple images taken over the course of many years. And to maximize efficiency, these surveys will observe in less than ideal conditions. The ability to directly measure and correct measurements for the variations of atmospheric transmittance will greatly improve the quality and scientific value of the archives produced by these future surveys.

The quality of the photometry of the present-day multi-epoch Sloan Digital Sky Survey (SDSS) has approached the precision needed for future surveys (Staughton et al. 2002) (Ivezic et al. 2004). The continuous and rapid observing cadence of this dedicated survey provided a measure of control over the stability of instrumental throughput, and allowed identification and analysis of varying observing conditions. Observing the sky in multiple epochs allowed the stability and uniformity of the internal calibration to be boot-strapped

from the repeated measurements of the magnitudes of the large number of stars contained in the survey fields. Selected SDSS data taken in good photometric conditions and analyzed with the so-called “Übercal” procedure, have indeed, reached 1% relative photometry (Ivezic et al. 2007) (Padmanabhan et al. 2008). But while the SDSS experience provides a limited proof-of-principle, calibration of future survey data will need to be done over still a wider range of observing conditions.

1.2. Deterministic Calibration of Imaging Surveys

It has been proposed (Stubbs & Tonry 2006) that the process of photometric calibration be separated into measurement of the atmospheric transmittance and independent measurement of the instrumental throughput. The concept is to directly measure the atmospheric transmittance $T^{atm}(alt, az, t, \lambda)$ with instrumentation dedicated to the task. This paper reports a study of a technique to implement part of this strategy in calibration of ground-based observations at optical and near-infrared (NIR) wavelengths.

The technique reported here takes advantage of state-of-the-art models of atmospheric optical radiation transport and readily-available codes to accurately compute atmospheric extinction over a wide range of observing conditions. The strategy is to repeatedly measure the spectra of a small catalog of bright “probe” stars as they progress across the sky and back-light the atmosphere during the night. This approach is made feasible by advances over the past several decades in understanding the makeup of the atmosphere and computer modeling of radiation transport. The signatures of various atmospheric constituents in these spectra include not only the wavelength dependence of optical absorption, but also characteristic dependences on airmass. It is not necessary to know the spectra of the probe stars *a priori* as they are determined from the data themselves after many observations over a wide range of airmass on differing nights. To cover the full optical and NIR range,

the catalog includes stars with a range of colors (G, F, A, and white dwarf). The efficiency of the spectrograph can also be determined from the observed spectra, and having a variety of spectra in the probe set helps break degeneracy between stellar parameters and the instrumental response.

This technique is suitable for application with present and future imaging surveys. It will provide excellent photometric calibration of data, and will extend the environmental conditions in which good photometric measurements can be made.

2. Atmospheric Transmittance of Light

Processes that attenuate light as it propagates through the atmosphere include absorption and scattering (Rayleigh) by molecular constituents (O_2 , O_3 , water vapor, and trace elements), scattering (Mie) by airborne macroscopic particulate aerosols with physical dimensions comparable to the wavelength of visible light, and shadowing by ice crystals and water droplets in clouds. Molecular scattering cross sections vary smoothly with the wavelength of the incident light, and the total molecular column thickness is proportional to barometric pressure and the airmass of the observation. Molecular absorption, on the other hand, is largely due to narrow saturated Lorentzian-shaped lines spaced closely together in wavelength. The curve-of-growth of a saturated line is nonlinear, and observations made with finite resolution (certainly the case for broad-band photometry) average the effects of many lines. This leads to intricate absorption spectra and to optical depths that do not scale linearly with airmass.

Shown in Figure 1 are a set of transmission functions for molecular components of the atmosphere calculated with the MODTRAN4(v3r1) computer code (Berk et al. 1999) that

is available from the U.S. Air Force Research Laboratory¹. The code computes transmission in wavelength increments of less than one Angstrom, but provides output binned with a user-defined resolution; the calculations shown in the figure are done for spectra measured with an instrument with resolution $R \equiv \lambda/\Delta\lambda \approx 400$ at $\lambda = 6500\text{\AA}$. Figure 2 shows how contributions to extinction from differing molecular components vary over a range of airmass values. The slope of the extinction line gives the power-law behavior of the optical depth, and the differing dynamics of the interactions between light and the atmospheric components can be seen in the figure.

Aerosols such as dust, sea salt, and man-made pollutants come in a variety of shapes and sizes that produce a range of dependences on the optical wavelength; smaller particulates produce stronger variations with wavelength. Ice crystals and water droplets in clouds have dimensions that are large compared to the wavelength of visible light, and produce shadows that appear as “gray” (i.e. wavelength independent) extinction.

2.1. The Fitting Model

The transmission functions shown in Figure 1 are for a particular composition of elements in the atmosphere, but we do not use this composition in our analysis that is discussed below. We use the code only to calculate spectral templates of transmission for each constituent of the atmosphere over the relevant range of airmass, and fit observations with a model for the atmospheric composition that best matches the computed templates. The goal is to use an efficient characterization of the important features of the atmosphere, and to fit a minimal set of parameters. Significant data has been gathered on the spatial and temporal structure of the constituents of the atmosphere (Stubbs et al. 2007), and

¹www.kirtland.af.mil

these guide the construction of our model.

Molecular oxygen, nitrogen, and trace elements are fully mixed gases, and the total vertical column height of these constituents is determined by barometric pressure. Each contributes to Rayleigh scattering (“*mols*”), and we combine their absorption lines into the single function “*mola*”; both are shown in Figure 1. We fit a single parameter for the entire data set that just calibrates the barometric pressure reading at the site on Cerro Tololo to the molecular templates computed with MODTRAN4. Absorption by these gaseous components scales approximately as the square root of the total number of molecules along the line of transport (Figure 2).

Absorption by ozone O_3 is shown separately in the figure. This element is the subject of extensive satellite monitoring campaigns aimed at better understanding weather and climate change.² Ozone above Cerro Pachon resides predominantly in the upper troposphere and lower stratosphere, and driven by jet stream winds, can vary 5-10% day-to-day around average values that exhibit season variations of 25% or so. We use a single parameter C_{O_3} for each observing night to account for this variation in our fits. Again this is just the ratio of the vertical column height of ozone at the time and place of the observation to that used in the MODTRAN4 calculation of the templates.

Aerosols are micron-sized particulates such as sea salt, smoke, and dust whose scattering cross sections scale less strongly with wavelength than does molecular Rayleigh scattering (i.e. typically as λ^{-1} versus λ^{-4}). These constituents are largely created at points on the earth’s surface, and are borne around the globe by winds in the lower troposphere. The density of aerosols at locales such as Cerro Pachon tends to be small and typically varies only slowly through a given night. But events such as storms or volcanic activity can

²www.toms.gsfc.nasa.gov.

produce significant changes in the vertical column height over periods of days to weeks. We model this contribution with a form that allows for spatial variations that are fit for each observing night, but the spatial variations observed in the data reported here are found to be rather small.

The content of precipitable water vapor is considerably more variable with fluctuations of 5-10% per hour possible. This constituent is not well-mixed, and ground-level relative humidity is not an accurate measure of the total column height. We find that the MODTRAN4 calculation of the spectral shape of absorption by water vapor to be sufficiently accurate, as is the prediction for dependence on airmass. But we find we must use a relatively rapidly time-varying coefficient C_{H_2O} to track changes sufficiently well for future surveys. It also proves necessary to allow for spatial variation across the sky. This spatial variation changes only slowly in time, however, so we compute corrections for target observations by interpolating between calibration measurements.

Water droplets and ice crystals in clouds have dimensions that are large compared to the wavelength of visible light, and so scattering of light in the visible and NIR bands is independent of wavelength (gray in color). Cloud cover is highly variable in both time and spatial direction. Successful fits to calibration spectra require a wavelength-independent “gray” normalization T_{gray} for each observation. Analysis and correction for this component of atmospheric extinction requires special care that is discussed below.

The fitting model for atmospheric transmittance of light used in this analysis is summarized with the formula:

$$\begin{aligned}
 T^{fit}(alt, az, t; \lambda) &= T_{gray} e^{(-z(alt) \cdot \tau_{aerosol}(alt, az, t; \lambda))} \times \\
 &\times (1.0 - C_{mol}(BP(t)/BP_0) A_{mols}(z(alt); \lambda)) \times \\
 &\times (1.0 - \sqrt{C_{mol} BP(t)/BP_0} A_{mola}(z(alt); \lambda)) \times \\
 &\times (1.0 - C_{O_3} A_{O_3}(z(alt); \lambda)) \times
 \end{aligned}$$

$$\times (1.0 - C_{H_2O}(alt, az, t)A_{H_2O}(z(alt); \lambda)). \quad (4)$$

The attenuation coefficients A_i are computed as one (1.0) minus the transmission templates computed with MODTRAN4 that are shown in Figure 1, and include all dependence on wavelength and airmass in the model. For practical reasons, these templates are precomputed in increments of 0.1 for the range of airmass encountered in the observing runs; values are then linearly interpolated to the airmass $z(alt)$ of individual observations. The barometric pressure $BP(t)$ is taken from the weather monitoring station at the site on Cerro Tololo, and is normalized to a reference value $BP_0 = 782\text{mb}$ typical of the site. The coefficients C_i are derived from fits to observed spectra as introduced above and discussed below.

The model expressed in Equation 4 includes only the specific instance of a vertical profile of atmospheric constituents contained in the MODTRAN model, and so does not include variations in multiple scattering or scintillation caused by atmospheric turbulence. This will be adequate to describe atmospheric extinction of images taken with exposure durations that average over sufficiently long times. This is not an issue for the analysis reported here, and in typical seeing conditions at observatories such as CTIO, should also be adequate for most existing or planned imaging surveys.

As mentioned above, the column thickness of water vapor varies in both space and time, and we approximate

$$C_{H_2O}(alt, az, t) = C_{H_2O}(t) + \frac{dC_{H_2O}}{dEW}\Delta EW + \frac{dC_{H_2O}}{dNS}\Delta NS, \quad (5)$$

where $EW = \cos(alt)\sin(az)$ and $NS = \cos(alt)\cos(az)$ are projections of the telescope pointing respectively in the east-west and north-south directions. The value at zenith $C_{H_2O}(t)$ is interpolated in time from values measured with calibration observations. We find that a single constant spatial gradient for each observing night fits the data well.

The aerosol vertical optical depth includes a fitted spectral index α , and allows for spatial variations. Specifically,

$$\tau_{aerosol}(alt, az, t; \lambda) = (\tau_0 + \tau_1 EW + \tau_2 NS) \left(\frac{\lambda}{\lambda_0} \right)^\alpha, \quad (6)$$

where $\lambda_0 = 6750\text{\AA}$ is chosen for convenience in the middle of the wavelength range of the observations, and EW and NS are defined as in Equation 5. The parameters α and τ_i are derived for each night of observing. Though it would be possible to include several aerosol constituents, we find satisfactory results with only a single component for the observing reported here.

3. Observing Campaign

We have carried out an observing campaign to provide data for development and test of the strategy reported in this paper. Observing was scheduled for five 3-night periods during the 2007 and 2008 seasons at the Cerro Tololo InterAmerican Observatory (CTIO) in northern Chile. No useful data were taken during one of these periods (June 2007) due to weather conditions on the mountain. A summary of the data used in the analysis reported here is given in Table 1.

3.1. Observing Strategy

The strategy we adopt is to utilize an observing cadence and pattern that will fully characterize the mix of atmospheric components along any line of sight on the sky at any time during a night of observing. The goal is to sample the line of sight (defined by hour angle HA and declination δ) as uniformly as possible, while also sampling individual stars as they rise and fall and are seen through a range of airmass. The procedure is essentially a sophisticated version of the standard observing technique of determining a nightly

extinction coefficient for a given bandpass from measurements of the broad-band flux at differing airmass (Equation 3). The advance here is to determine each of the absorption coefficients defined in Equation 4 by observing how spectra of stars change as the airmass and observing direction change throughout the night. The extrapolation to the top of the atmosphere is then computed entirely from the MODTRAN4 templates.

The target stars used in this study and their magnitudes and types are given in Table 2. These were chosen to provide good coverage of the sky throughout the nights of observing, and to have spectra with complementary coverage in wavelength. The blue spectra of hot DA white dwarf targets contrast with the cooler spectra of F-stars, and so provide useful constraints on fits to features of atmospheric transmission. Yet both are relatively smooth and free of strong features (Balmer lines are easily modeled in the fitted spectra). Several are Southern spectro-photometric standards (Hamuy et al. 1994). These were included to facilitate the initial reduction of the spectra by IRAF, but as discussed below, the analysis of atmospheric extinction does not require prior knowledge of the magnitudes or spectra of the targets.

The observing sequence and cadence used in these studies were chosen largely in real time by the observer in the control room. An approximate plan was drawn up prior to the start of observing each night, but the choice of which target was observed at a given time was not pre-programmed. The maximum airmass at which stars were observed was limited to 2.0 by the range of the telescope, but attention was paid to take spectra of stars as they were near this limit either on the rise or fall. Sets of two or three spectra were taken of a star at each pointing of the telescope, so the total time spent at one point on the sky before slewing to another point was typically 10 minutes. Data were taken as long as stars could be seen on the telescope guide camera. A plot in (HA, δ) of the pointing for one night of observing is shown in Figure 5.

3.2. Data Collection and Reduction

All results reported here are based on observing done with the SMARTS 1.5m Cassegrain telescope at CTIO on Cerro Tololo. Data were taken with the Ritchey-Chrétien spectrograph (RC-SPEC) using two different grating tilts and corresponding blocking filters. A “red” instrumental setup employed a low-dispersion grating (RC-SPEC#11) at 12.5 degree tilt blazed at 8000Å. All observing was done in first order with an OG530 blocking filter to eliminate second-order light at wavelengths below 10500Å. This resulted in a dispersion of 5.4Å/pixel on the CCD and FWHM resolution of 16.4 Å. The resolution of the spectrograph in this configuration is $R \approx 400$ at 6500Å, as used in the MODTRAN4 calculations of the fitting templates. A “blue” setup used the same grating at 11.8 degree tilt and a GG385 blocking filter to obtain a free spectral range of 4000Å to 7500Å. In this configuration the scale dispersion is 6.5Å/pixel.

The magnitudes of stars chosen for this study (see below) are in the range $9 < V < 12$, and exposure times from 120 secs to 240 secs were used to acquire spectra. This resulted in single-channel counts of a few hundred at the extremes of the free spectral range for the faintest stars to $\geq 20,000$ ADU in the middle of the range for the brightest stars. The efficiency of the sensor in the spectrograph falls rapidly redward of 9000Å, and as discussed below, statistical errors in measurements made at these longer wavelengths grow appreciably.

The slit on RCSPEC does not rotate to track the parallactic angle of refraction, so all spectra used here were taken with either a 10 arcsec or 15 arcsec full aperture. Target stars were first visually centered with the slit closed to 1 arcsec, then the slit was opened to acquire spectra. Atmospheric seeing during these observations was typically 1 arcsec and less than 2 arcsec in the worst cases. Calculations (Filippenko 1982) indicate that, with these conditions and for the range of telescope pointing, these aperture widths suffice to

avoid bias in the observed spectra due to atmospheric dispersion. The probe stars were all chosen to be well-isolated from other bright sources to avoid confusion in these wide slit apertures. No difference was seen between results derived from spectra taken with the two settings of the slit.

Bias frames and dome flats were taken daily and used in reductions of the 2-d CCD images of the slit. Quartz lamp flats and neon lamp calibration exposures were taken with each new pointing of the telescope. Spectro-photometric standards were included in the target sets. Reductions of 2-d images to 1-d spectra were performed with IRAF software³, and included overscan and bias removal, sky subtraction, and wavelength calibration. A first correction of the spectra for instrumental signature and flux calibration was done using the available standard targets, but no extinction corrections were applied. This step is done largely for convenience since these calibrations are finally determined in the atmospheric fitting process described below; but doing so at this point improves the efficiency of the final fitting. The CCD detector on the spectrograph exhibits significant fringing at the longer wavelengths. This effect is partially removed by the flat-field correction applied during the reductions, and further reduced in the summation of spectra to produce synthetic broad-band magnitudes. Reductions were done separately for each distinct observing period during the campaign, but the same pipeline was used for all data. Several examples of reduced 1-d spectra are shown in Figures 3 and 4.

To provide control and checks in the analysis, the data were separated into a set of observations used to calibrate the atmospheric extinction, and a disjoint set used for blind tests of the results of the calibration. There were four stars that were visible during

³IRAF software is distributed by the National Optical Astronomy Observatory, which is operated by the Association of Universities for Research in Astronomy (AURA) under cooperative agreement with the National Science Foundation.

more than one of the runs (Table 2). Observations of these stars were used to calibrate the spectrograph instrument response and to fit slowly varying terms in the atmospheric extinction. The calibration data set was broadened to include observations of several of the remaining stars in order to fit the more rapidly varying water vapor. These were initially chosen to provide measurements at approximately hourly intervals during each night. This interval was found to be too sparse to determine sufficiently well the temporal variation of the water vapor during the nights we observed, so the number of calibration observations was increased to reduce the interval between points to ≤ 20 minutes. This is an important conclusion of our study.

3.3. Fitting Procedure

Analysis of the data consisted of a single iterative fit to the entire set of observations. The fit included parameters that define the spectra of each of the target stars, parameters that refine the instrument calibration (one per observing night), and the coefficients of the atmospheric model defined above. Two types of fits were used to optimize sensitivity to the different parameters. A Kolmogorov-Smirnov (KS) goodness-of-fit parameter was computed as the maximum of the absolute value of the difference between the cumulative observed spectrum and the cumulative model spectrum each normalized to unity over the range of wavelengths included in the fit. The KS parameter was computed for each observed spectrum and the model for that observation, and a single global KS statistic then computed as the mean of the individual goodness-of-fit parameters computed over the entire data set. We do not interpret the KS parameter in a probabilistic sense; it is only used as a tool for finding a good description of the observations.

The global statistic was used to fit the effective temperature and surface gravity of each target star, the instrument efficiency for each night, and atmospheric constituents

with extinctions that vary slowly with wavelength - the one scale parameter for molecular scattering and absorption C_{mol} , the thickness of ozone C_{O_3} for each night, and the nightly parameters that describe the aerosol extinction. This technique eliminates the need to model errors to determine these parameters, and is independent of “gray” cloud conditions that effect only the normalization of the observed spectra. The water vapor content in the atmosphere and the normalization of the spectra T_{gray} were fit for each observation with a chi-square computed with statistical errors estimated from raw counts in the unreduced 2-d images. These techniques were used iteratively.

The procedure initially set the coefficients of the atmospheric model to default values, and started with the instrument correction left as determined during the initial IRAF reductions of the 2-d spectra. A first set of parameters was fitted for the spectra of the four stars that were visible during more than one observing run. Models (Kurucz 1993) were taken for the main sequence stars, and blackbody spectra with Lorentzian Balmer lines used for white dwarfs. The effective temperature T_{eff} , surface gravity $\log(g)$, and luminosity were fitted to the calibration observations, as were the widths and depth of Balmer lines. The main-sequence models are given in (Kurucz 1993) as tables of discrete values of T_{eff} and $\log(g)$; the model spectra were linearly interpolated in each wavelength bin to yield the best fits. Metallicities were set to solar values.

A smoothing function was used to refine the instrument response for each night. As discussed above, particular observations of standard stars were used to initially normalize all other spectra taken on a given night. This procedure avoids regions affected by Telluric lines, but will imprint a particular instance of the continuous part of atmospheric extinction on the initial normalization. The fitted smoothing function removes this bias since it is constrained to describe spectra taken of each probe star over a range of airmass. The consistency of the fit was confirmed after the full iterative procedure was completed.

The slowly varying (nightly) atmospheric coefficients were fit using spectra of the four stars that were observed during more than one run of the campaign. The parameters of the remaining stars in the target list were then determined, and finally the water vapor and gray cloud extinctions were fitted with the chi-square statistic.

A second overall iteration was done with a single simultaneous optimization of the global KS statistic, followed by a final single chi-square fit to the water vapor and normalizations. After two iterations, the solution was found to be stable to statistical precisions consistent with those estimated from the raw counts in the observed spectra. The luminosity of each target star was ultimately determined from the brightest value found in the set of observations, and the values of T_{gray} were renormalized by the brightest observation of a given star (i.e. they were all rescaled to be no greater than unity).

As a test of the robustness of the final solution, the instrument efficiencies were varied arbitrarily around their fitted values. It was found that local (i.e. wavelength dependent) variations of more than 1% made it impossible to obtain best-fit solutions for the atmospheric parameters at all airmass. This was borne out both by visual inspection of the fits and in the goodness-of-fit statistics used in the fitting process. The overall slope of the instrument efficiency is degenerate with a common change in the effective temperatures of *all* stars in the fit. This degeneracy was arbitrarily broken by minimizing the deviation of the normalization of the instrument efficiency from that determined with the initial IRAF standardization. This process does not change the wavelength-by-wavelength product of the instrument calibration and the probe star spectra, and since our goal is to determine the atmospheric parameters, not stellar properties, this is acceptable.

4. Results

The fit described above yielded the single parameter $C_{mol} = 0.910$, and the slowly varying atmospheric parameters C_{O3} , τ_i , and α given in Table 3. Values for T_{gray} and C_{H2O} for all observations of calibration stars are shown in Figures 6 and 7. An overall chi-square per degree of freedom (DOF) can be computed from the final fit even though the chi-square statistic was only used for a portion of the fitting process. This gives a value $\chi^2/\text{DOF} = 1.55$ for 181406 degrees of freedom after clipping outliers at 5σ .

The aerosol concentrations (τ_0) are seen to vary by an order of magnitude or so, but the values are within historically typical values (Gutierrez-Moreno et al. 1986) (Burki et al. 1995). The single-order spectrographic measurements cover only a factor of two in wavelength, so uncertainty in the spectral index α of the aerosol is large and estimated by variation of parameters and use of the chi-square to be $\delta\alpha \sim 0.5$. The fitted values are consistent with those that have been historically found at these and similar sites. The mean ozone concentration is seen to be consistent with the MODTRAN4 default value (338 Dobson), and to display the expected seasonal variation, though the best value on the night of April 26, 2008 is somewhat high. The limited wavelength coverage of the fitted range of spectra taken with the Red set-up (5500Å - 10000Å) leaves some ambiguity between the ozone level and the spectral function of the aerosol. The airmass dependence of these two components is nearly identical (Figure 2), however, so the computed broad-band extinction is rather insensitive to this ambiguity.

The precipitable water vapor is seen in Figure 7 to have varied in time by significant amounts. There were both slow trends, and also rapid changes over times of order an hour or so. The ground level relative humidity is seen to not be a useful proxy for the total vertical column height of water vapor. So the coefficients that define the vertical column height $C_{H2O}(t)$ (Equation 5) determined from the calibration observations were interpolated

to obtain values of for all non-calibration observations. For these observing nights, we found it necessary to choose calibration points at intervals ≤ 20 minutes apart to measure y -band magnitudes with sub-percent repeatability.

We also looked for spatial variation in the atmospheric water vapor. This was done by computing the difference in C_{H_2O} for sequentially observed spectra. Shown in Figure 8 is the change in water vapor plotted against the change in the east-west pointing of the telescope (δEW) for two runs of the campaign. There are groups of points near $\delta EW = 0$ in both sets of data that correspond to the repeated spectra of the same star taken following each slew of the telescope. The distribution of these points gives an estimate of the measurement error of $\delta C_{H_2O}(\text{rms}) \approx 0.02$ for both data sets. The remaining points are those computed from the last spectrum taken at one pointing and the first spectrum taken after a slew of the telescope. It can be seen that there was a clear and steady east-to-west increase in the water vapor content taken in November 2007. Such a trend is not seen in data from the earlier April run, nor was any other spatial dependence seen in any of the data. There is a more rapid variation with position that is statistically greater than the measurement error seen in most of the data. But the magnitude of this higher frequency component produces less than 0.1% of residual scatter in the corrected y -band magnitudes, so we ignore it in this analysis. We used the form given in Equation 5 with a fixed gradient $dC_{H_2O}/dEW = 0.166$ for this run.

We interpret the “gray” opacity as cloud cover, but though plausible, that interpretation is not essential to the analysis. The gray opacity is just the wavelength independent portion of the extinction. It varies from observation to observation by several per cent, and since the recorded distribution is biased to those points in time when clouds did not prevent a spectrum from being taken, the actual variation is greater. The spatial structure can be quite complex, and that too shows through in the data reported here. This is discussed

further below, but to proceed, we separate presentation of “gray” extinction from chromatic terms that depend on wavelength.

Table 3 also includes data taken in April 2007 with the blue tilt of the spectrograph. This setup allows synthesis and analysis of the g and r bands. As in the later runs, the analysis favors presence of a weak aerosol component in the atmosphere that was spatially uniform and stable during the observing period. The ozone concentration was similarly consistent with the later runs.

5. Discussion

We present our results in the form of synthesized broad-band photometric magnitudes and colors. For this purpose a set of hypothetical instrumental throughput functions $T_{b,syn}^{inst}(\lambda)$ are defined for filters $b = grizy$ similar to those used in SDSS and planned for DES and LSST. The shortest optical wavelengths were not accessible with the setups of the spectrograph used for these studies, so no results for bluer filter bands, e.g. u-band, are given here. These synthetic test functions are shown in Figure 9. The y -band chosen here provides a very stringent test as it includes the range 9000Å - 10000Å where there is strong absorption by water vapor.

We follow the SDSS convention and define a measured broadband magnitude of a celestial source as (Fukugita et al. 1996),

$$m_b^{meas} \equiv -2.5 \log_{10} \left(\frac{ADU_b^{meas}}{A \Delta T \int_0^\infty \lambda^{-1} F_{AB} T_b(\lambda) d\lambda} \right), \quad (7)$$

where the measured number of counts ADU_b^{meas} is defined in Equation 1 by the true source flux and the unknown actual observational bandpass. The SDSS magnitude is normalized by a standard observational bandpass and a flat SED $F_{AB} = 3631$ Jy (1 Jansky = 10^{-23} erg cm^{-2} s^{-1} Hz^{-1}).

To compute a synthesized magnitude from the observed spectra and the fitted parameters, the following steps are taken:

- Each observed spectrum is corrected for the fitted RCSPEC instrumental throughput extracted from the nightly fits to yield the flux that reaches the input pupil of the telescope $F_\nu^{pupil}(alt, az, t, \lambda)$. (Note that the spectra shown in Figure 3 and Figure 4 are $F_\lambda(\lambda) = cF_\nu(\lambda)/\lambda^2$.)
- Synthesized instrumental magnitudes are computed by summing bin-by-bin in wavelength,

$$m_b^{syn} = -2.5 \log_{10} \frac{\int_0^\infty F_\nu^{pupil}(\lambda) T_{b,syn}^{inst}(\lambda) \lambda^{-1} d\lambda}{\int_0^\infty T_{b,syn}^{inst}(\lambda) \lambda^{-1} d\lambda} - 48.60, \quad (8)$$

where the zero point is computed for F_{AB} expressed in $\text{erg cm}^{-2} \text{ s}^{-1} \text{ Hz}^{-1}$.

- The atmospheric transmission $T^{fit}(alt, az, t, \lambda)$ is computed with Equation 4 and the appropriate parameters from the calibration fits.
- An equivalent atmospheric extinction is computed as,

$$E_b = -2.5 \log_{10} \frac{\int_0^\infty T^{fit}(\lambda) T_{b,syn}^{inst}(\lambda) \lambda^{-1} d\lambda}{\int_0^\infty T_{b,syn}^{inst}(\lambda) \lambda^{-1} d\lambda} \quad (9)$$

This is the photon-weighted atmospheric extinction averaged over the test instrumental bandpass b for a source with a flat SED.

- The corrected *top-of-the-atmosphere* source magnitude is then computed,

$$m_b^{TOA} = m_b^{syn} - E_b = -2.5 \log_{10} \frac{\int_0^\infty F_\nu^{pupil}(\lambda) T_{b,syn}^{inst}(\lambda) \lambda^{-1} d\lambda}{\int_0^\infty T^{fit}(\lambda) T_{b,syn}^{inst}(\lambda) \lambda^{-1} d\lambda} - 48.60 \quad (10)$$

Colors are computed as differences of these source magnitudes. Equation 10 essentially mimics a set of observations made with a perfectly known instrumental bandpass weighted with the fitted atmospheric transmittance. This formulation isolates the effects of the atmosphere in terms most directly related to ground-based astronomical observations.

5.1. Synthetic Photometric Analysis

For demonstration purposes, we first compute the extinction due to only the “non-gray” attenuation processes in the atmosphere (i.e. Equation 9 evaluated with T^{fit}/T_{gray}). A set of histories of such extinction values are shown in Figure 10 for calibration observations made in the *rizy* bands. It can be seen that while atmospheric extinction in the *r* band exhibits a stable linear dependence on airmass (i.e. Equation 3 is a good approximation), the varying water vapor yields a complex behavior at the longer wavelengths. Clearly using a single linear dependence on airmass to compute extinction through the night will lead to large errors in the redder bands. The *y* band correction varied over this one night by as much as 50 millimag (peak-to-peak) at fixed airmass. This behavior is typical for the data reported here.

As a measure of the internal precision of the calibration, we next compute the top-of-the-atmosphere magnitudes (i.e. Equation 10) for each of the calibration observations using all the information available (i.e. including the “gray” term). The dispersions of these values for each night of the campaign are given in Table 4, and the distribution of data from all nights of the campaign is shown in Figure 11. The rms values of the residuals are found to range from 0.002 to 0.004 magnitudes in *griz*, and 0.0055 to 0.0075 in *y*-band. These can be compared with the precision of the data estimated from the statistical counts in the spectra to be 0.002 in *gri*, 0.003 in *z*, and 0.005 in *y*. Residual contributions due to errors in the atmospheric model, the fitting procedure, and sampling limitations are seen to be most significant in the *y*-band where they are comparable to the statistical error.

Next we look at the observations of the stars used as blind test sources. Shown in Figures 12, 13, and 14 are plots that summarize the analysis of blind observations that are not included in the calibration fit. In each case, the magnitude or color derived for the observation is compared to the corresponding average quantity for the set of observations

from the same star. If we assume that no correction can be made for “gray” extinction, then the residual (Figure 12) reflects the variation seen in the temporal plot of cloud cover (Figure 6). Clear correlations in T_{gray} from point to point in time can be seen in Figure 6, and some improvement can be gained by interpolating between calibration observations to other points in space and time as done with the water vapor corrections. There is a set of observations for which this makes a substantial improvement. But the spatial structure of the cloud cover is such that a correction computed from a spectrum taken at one time or location can not be used to accurately correct an observation taken at different times or elsewhere.

To examine the completeness of our model of atmospheric extinction we “cheat” and use the values of T_{gray} that are extracted from fits to the blind observations of the probe stars. These “gray-corrected” residuals are shown in Figure 13, and the values of the residuals are given in Table 4. It is evident that all other calibration factors transfer accurately to the blind observations in the *griz* bands, with some degradation in the *y* band. As a further test we look at colors computed as differences of magnitudes derived from the same observed spectrum; these will be independent of true “gray” extinction. The dispersion of colors computed from blind observations are shown in Figure 14. These color dispersions are somewhat smaller than would be expected if the residual errors in separate bands are independent. This is consistent with there being remaining errors in the atmospheric model that introduce correlated errors in the individual band magnitudes. But the consistency of the dispersion of the corrected magnitudes and the color magnitudes leads to the important conclusion that *our model accounts for all contributions to extinction larger than ~ 3 millimagnitudes in these data.*

6. Conclusions

We have constructed a model for transmission of light from the top of the atmosphere to ground that accurately describes observations made during the nights of this study. The model includes all significant components of the atmosphere that contribute to the extinction of light. The signatures of these components in observed spectra of stars can be computed accurately, and repeated measurements of the spectra of stars as they traverse the sky can be analyzed to extract the parameters of the model. Chromatic (non-gray) extinction can be evaluated from the model for arbitrary coordinates on the sky and times during any night included in the calibration. The fidelity of the computed signatures makes it possible to determine the parameters with good accuracy. Scattering and absorption processes that cause 5-20% loss of the light at optical wavelengths can be measured with 2-3% accuracy to leave residual errors that are below 0.5%. The calibration is limited by a rapidly changing “gray” extinction that is consistent with moving and evolving cloud cover.

Specific results for the data used in this study are given in Tables 3 and 4, and in Figures 6 and 7. The atmospheric parameters summarized in Table 3 are consistent with typical seasonal variations (see e.g. (Stubbs et al. 2007), and references therein), and dispersions of the extinction measured in different observing periods and with different data samples are internally consistent. The observed magnitude dispersions are, not surprisingly, greatest in the y band. This is due in part to poor efficiency at the longer wavelengths of the spectrograph used in these studies, and in part to remaining unaccounted variations in the water vapor column height. We note also that observed r band dispersions are larger than those in g and i , and particularly $r - i$ color dispersions are consistently larger than dispersions of $i - z$ color. Dispersions in g and i are consistent with expected statistical errors, while the r band measurements are slightly larger. This may be due to modeled temporal or spatial variation in the ozone layer that would have greatest effect in the r

band.

It is important to note that we have not addressed the accuracy of the photometric zero-points, nor the accuracy of measured colors. Our results show that, if the cloud cover can be measured separately, then the calibration method used here can provide sub-percent precision defined as the reproducibility of measured magnitudes *at the top of the atmosphere* of individual celestial objects. Calibration of absolute broad-band scales will require different techniques. Proposals have been made to use observations of well characterized white dwarf stars (Holberg & Bergeron 2006), or analysis of the color distributions of main sequence stars (MacDonald et al. 2004) (Ivezic et al. 2007) (Sale et al. 2009) (High et al. 2009) for this purpose.

6.1. Design of Future Surveys, Cloud Shadows and Gray Extinction

We have presented a strategy that is suitable for implementation at observatories that host dedicated all-sky survey telescopes (e.g. LSST (Ivezic et al. 2009)), or could be used to more accurately correct spectra taken with existing instruments. We have carried out an observing campaign with existing telescopes that validates this approach. We note that the technique will benefit greatly from improved sensors now becoming available with good efficiency at near infrared wavelengths, and from multi-order spectrographs that permit simultaneous data to be taken over larger ranges in wavelength. Simultaneous measurement of spectra between 4000Å and 10500Å will provide significantly improved resolution of the parameters of aerosols, and clear definition of the main ozone feature between 5000Å and 7000Å. As is evident from the studies here, the resolution of the spectrograph need not be high as even modest resolution suffices to cleanly pick out key molecular absorption features. It seems likely that more detail can be included in the extinction model (Equation 4) used to describe the larger and more consistent data sets that will be acquired during future

surveys.

Calibration of broad-band imaging survey data requires that we also be able to correct for the gray (wavelength independent) extinction produced by water droplets and ice crystals in clouds. Cloud structure can be intricate with significant spatial variations across a single field of view, and can change in the interval between exposures. In the worst case, the loss of light will be too severe to allow useful data to be taken. But it will be important to be able to correct data for thin cloud cover that may not be apparent to the naked eye, and it will certainly be of great benefit to be able to take useful data over an extended range of atmospheric conditions. There are several important features of future dedicated surveys that should enable this to be done. These surveys will use telescopes with large fields of view several degrees across, and they all will be sensitive enough to capture several tens of thousands of stars in each image. These surveys also will observe these stars multiple times, and so will be sensitive to changes from ideal observing conditions.

We would seek a calibration of each image relative to a “best” reference condition of the sky encountered during the survey. Absolute calibration of this reference condition would then be a second step. A possible strategy would be to utilize a catalog of objects, mostly stars, constructed from the survey images themselves. The number of such sources on each image will be sufficient to create a map of T_{gray} across each image with spatial resolutions of a few arc minutes. Magnitudes for each of these point-like objects would be first corrected for chromatic extinction using the technique discussed in this paper. A specific implementation could include color corrections to approximately account for slopes of the object SEDs across standardized bandpasses defined for the survey. An effective light curve would then be constructed for each star from the repeated observations of it, and a gray extinction defined for each observation by normalizing to the brightest observation made in the appropriate bandpass. As illustrated in Figure 12, with a sufficiently large data

sample taken at sites typical of astronomical observatories, there will be a subset of the data that will be taken in truly “photometric” conditions. These conditions will constitute a reference observational bandpass for the survey that will be defined by the magnitudes of the reference stars.

It remains to determine the range of atmospheric conditions in which good photometric precision can be maintained with the technique suggested here. As part of the campaign described in this paper, we acquired data to address this question. We took spectra of our probe stars with the SMARTS 1.5m telescope simultaneously with acquisition of imaging data with the SMARTS 0.9m telescope on one occasion (Smith et al. 2008), and the Blanco 4m telescope on another occasion (Burke et al. 2009). Analysis of those data is underway, and will be the subject of a subsequent paper.

This work has been done as part of the design and development activity of the Large Synoptic Survey Telescope (LSST). The LSST is supported by the National Science Foundation under Scientific Program Order No. 9 (AST-0551161) through Cooperative Agreement AST-0132798, and under Department of Energy contracts DE-AC02-76SF00515, DE-AC02-98Ch10886, DE-FG02-91ER40, DE-FG02-91ER40677, and W-7405-Eng-48. Additional funding comes from private donations, in-kind support at Department of Energy laboratories and other LSSTC Institutional Members.

Facilities: SMARTS 1.5m Cassagrain Spectrograph.

REFERENCES

- Berk, A., et al. 1999, Proceedings of the SPIE, 3756, 348
- Burke, D.L., Axelrod, T., Claver, C., DePoy, D., Saha, A., Smith, C., Stubbs, C., & Tucker, D. 2009, CTIO Proposal 09A-0114
- Burki, G., Rufener, F., Burnet, M., Richard, C., Blecha, A., & Bratschi, P. 1995, A&AS, 112, 383
- Filippenko, A. 1982, PASP, 94, 715
- Flaugher, B., DES Collaboration 2007, BAAS, 209, 22.01
- Fukugita, M., Ichikawa, T., Gunn, J.E., Doi, M., Shimasaku, K., & Schneider, D.P. 1996, AJ, 111, 1748
- Glazebrook K., Peacock J.A., Collins, & Miller, L. 1994, MNRAS, 266, 65
- Gutierrez-Moreno, A., Moreno, H., & Cortes, G. 1986, PASP, 98, 1208
- Hamuy, M., Suntzeff, N.B., Heathcote, S.R., Walker, A.R., Gigoux, P., & Phillips, M.M. 1994, PASP, 106, 566
- High, F.W., Stubbs, C. W., Rest, A., Stalder, B., Challis, & P. 2009, AJ, 138, 110
- Holberg, J. B. & Bergeron, P 2006, AJ, 132, 1221
- Ivezic, Z., et al. 2004, Astron. Nachr./AN, 325
- Ivezic, Z., et al. 2007, AJ, 134, 973
- Ivezic, Z., et al. 2008, astro-ph/0805.2366
- Kaiser, N., Aussel, H., & Burke, B.G. 2002, Proceedings of the SPIE, 4836, 154

- Kurucz, R. L., 1979, ApJ Suppl., 40, 1
- Landolt, A. U. 1992, AJ, 104, 340
- MacDonald, E.C., et al. 2004, MNRAS, 352, 1255
- Magnier, E.A. & Cuillandre, J.-C. 2004, PASP, 116, 449
- Manfroid, J. 1996, A&AS, 118, 391
- Marshall, J.L. & DePoy, D.L. 2005, astro-ph/0510233
- Padmanabhan, N, et al. 2008, ApJ, 674, 1217
- Regnault, N., et al. 2009, A&A, 506, 999
- Sale, S.E., et al. 2009, MNRAS, 392, 497
- Smith, C., et al. 2008, CTIO Proposal 08A-0477
- Stoughton, C., et al. 2002, AJ, 123, 485
- Sterken, Ch, Ed., “The Future of Photometric, Spectrophotometric and Polarimetric Standardization” 2006, PASP Conf Series 364
- Stetson, P. B. 2005, PASP, 117, 563
- Stubbs, Christopher W. & Tonry, John L. 2006, ApJ, 646, 1436
- Stubbs, C., et al. 2007, PASP, 119, 1163

Table 1: Periods of Observation.

Dates (nights)	Spectograph Tilt	Spectral Range (Angstroms)	Filters	Observing (hours)	Spectra (number)
Apr 24, 2007	Blue	4000 - 6800	g, r	9	41
Nov 2-3, 2007	Red	5500 - 10000	r, i, z, y	17	111
Apr 24-26, 2008	Red	5500 - 10000	r, i, z, y	22	262
July 23, 2008	Red	5500 - 10000	r, i, z, y	8	94

Table 2: Target Stars Used to Back-Light the Atmosphere.

Star	Magnitude (V)	Type	RA (J2000)	DEC (J2000)	Observations
CD-34241	11.2	F	00 41 47	-33 39 08	Nov
CD-35534	10.0	F	01 32 04	-34 29 15	Nov and July
HD 24954	9.9	F	03 56 10	-41 35 42	Nov
CD-277546	9.5	F	10 35 08	-28 22 38	Apr
HD 103441	9.4	F	11 54 36	-54 43 57	Apr
HD 113815	9.7	F	13 06 21	-02 46 33	Apr
CD-329927	10.4	A	14 11 46	-33 03 14	Apr and July
HD 145330	9.9	F	16 10 45	-10 32 18	Apr
EG 274	11.0	DA	16 23 34	-39 13 46	Apr and July
LTT 7379	10.2	G	18 36 26	-44 18 37	July
HD 189910	9.6	F	20 03 18	-25 08 45	July
HD 207474	9.6	F	21 49 10	-02 02 24	July
LTT 9239	12.1	G	22 52 41	-20 35 33	Nov and July
Feige 110	11.8	DA	23 19 58	-05 09 56	Nov
CD-761164	10.1	A	23 26 55	-75 38 29	July

Table 3: Summary of Calibration Fit Results

Date	C_{O_3}	$\tau_0(\%)$	$\tau_1(\%)$	$\tau_2(\%)$	α
Apr 24, 2007	0.83	1.5	0.00	0.00	-0.94
Nov 2, 2007	0.80	3.9	0.02	-0.03	-1.70
Nov 3, 2007	0.90	5.6	0.01	-0.01	-0.95
Apr 24, 2008	0.86	1.2	0.00	0.00	-0.50
Apr 25, 2008	1.04	0.8	0.00	0.00	-1.10
Apr 26, 2008	1.46	0.8	0.00	-0.00	-1.50
Jul 23, 2008	1.32	0.0	NA	NA	NA

Table 4: Summary of Gray-Corrected Dispersion Measurements

Data Set	Band or Color								
	g	$g - r$	r	$r - i$	i	$i - z$	z	$z - y$	y
	(rms magnitude 10^{-3})								
April07 Calibration Magnitude	2.3	...	4.0
April07 Blind Magnitude	1.6	...	3.8
Nov07 Calibration Magnitude	2.2	...	1.9	...	2.6		7.5
Nov07 Blind Magnitude	4.0	...	3.3	...	3.7	...	7.1
April08 Calibration Magnitude	2.8	...	3.2	...	3.6	...	5.5
April08 Blind Magnitude	3.3	...	2.8	...	3.1	...	7.9
July08 Calibration Magnitude	2.2	...	2.2	...	3.8	...	5.5
July08 Blind Magnitude	2.4	...	2.0	...	3.2	...	6.5
April07 Color	...	5.1
Nov07 Color	2.1	...	1.6	...	6.4	...
April08 Color	4.0	...	1.6	...	6.4	...
July08 Color	2.9	...	2.4	...	4.0	...

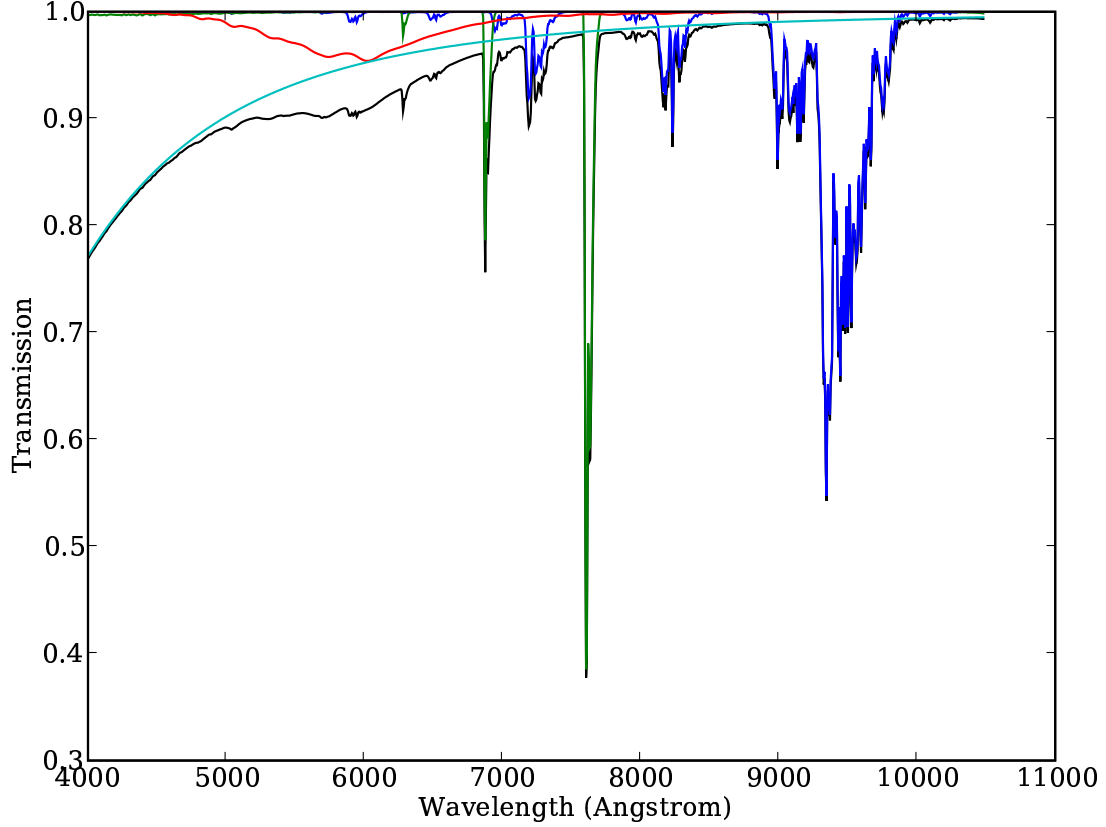


Fig. 1.— Computed optical transmission at zenith from Tololo to space. The atmospheric mix used in the calculation is the 1976 U.S. Standard option in MODTRAN4. Absorption by ozone A_{O_3} (red) and water vapor A_{H_2O} (blue) are shown separately, while contributions of oxygen and a number of trace elements are combined into one function A_{mola} (green). Rayleigh scattering A_{mols} by these molecular constituents is also shown (light blue). The total transmission through these constituents is shown as a black line. The plot includes no contributions from aerosols or clouds.

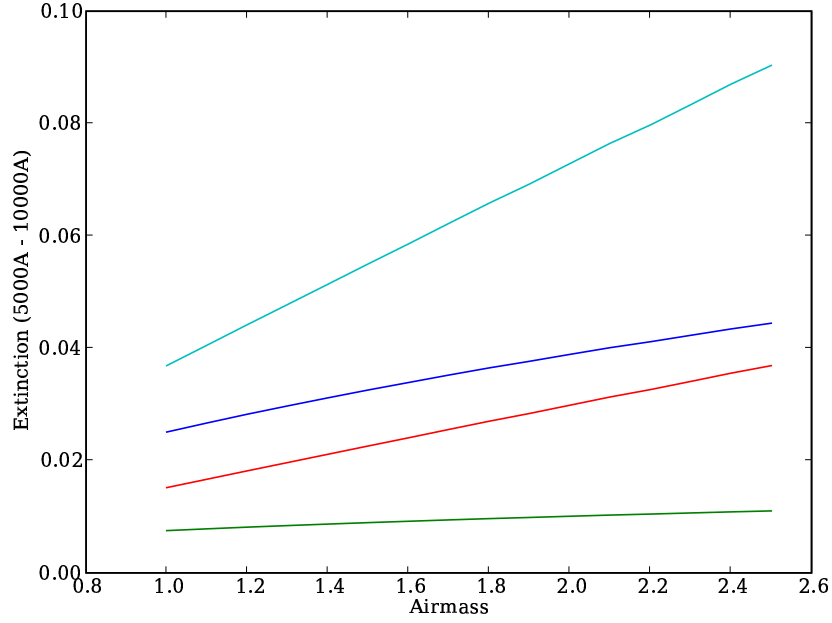


Fig. 2.— Contribution to extinction (magnitudes) from various components in the atmosphere: oxygen (green), ozone (red), water vapor (blue) and Rayleigh scattering (light blue) for the 1976 U.S. Standard mix. The extinction is computed over the range 5000Å to 10000Å for a source with a flat SED. The slopes of the extinction lines correspond to nearly linear dependence of optical depth with airmass for ozone (slope = 0.97) and Rayleigh scattering (slope = 0.98), while the oxygen and water vapor slopes are 0.59 and 0.71 respectively.

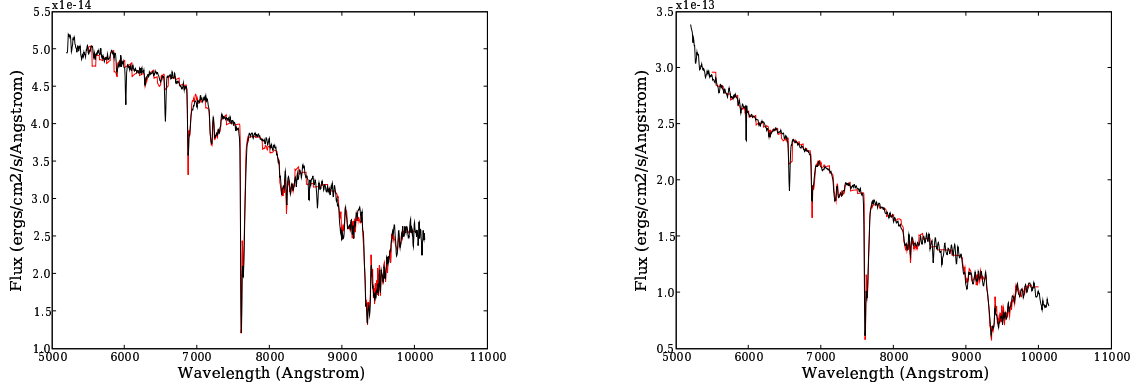


Fig. 3.— Spectrum of the G-star LTT 9239 taken at 1.57 airmass on November 3, 2007 (left). Spectrum of the F-star CD-35 534 taken at 1.50 airmass on July 23, 2008 (right). The flux is $F_{\lambda}(\lambda)$ ($\text{ergs cm}^{-2} \text{ s}^{-1} \text{ \AA}^{-1}$), and the fitted spectra are overlaid in red in both cases.

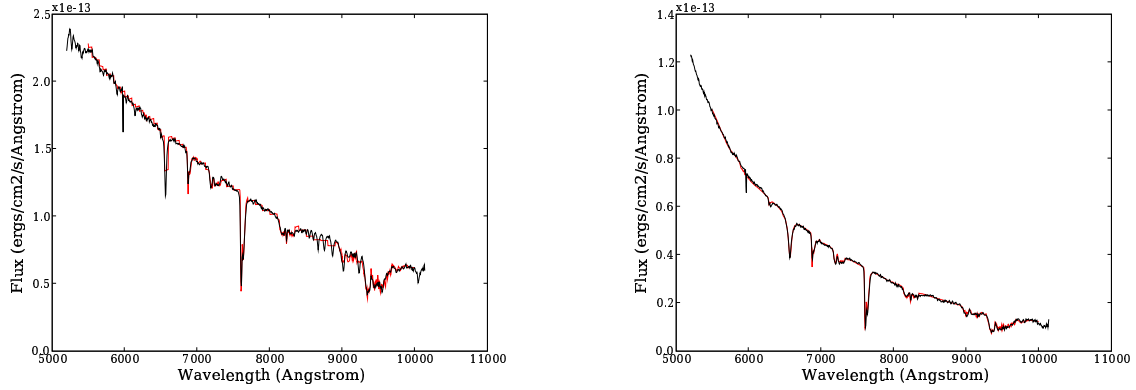


Fig. 4.— Spectrum of the A-star CD-32 9927 taken at 1.03 airmass on April 26, 2008 (left). Spectrum of the white dwarf EG274 taken at 1.94 airmass on July 23, 2008 (right). The flux is $F_{\lambda}(\lambda)$ ($\text{ergs cm}^{-2} \text{ s}^{-1} \text{ \AA}^{-1}$), and the fitted spectra are overlaid in red in both cases.

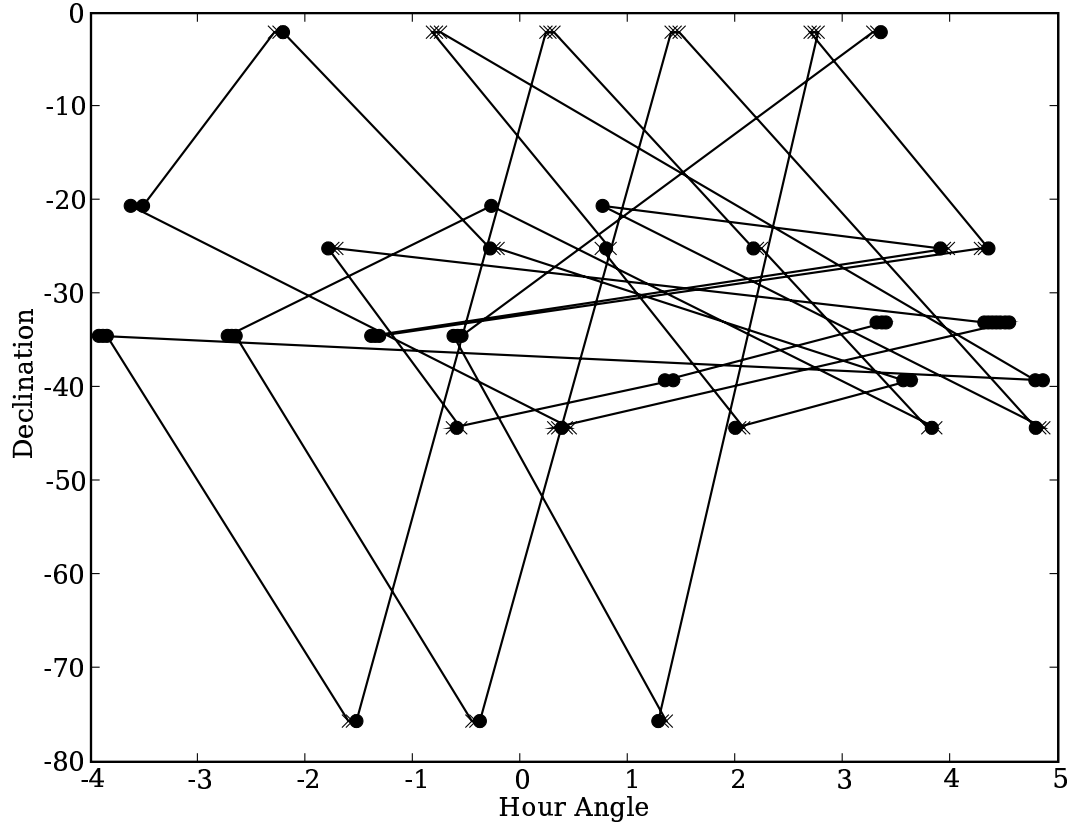


Fig. 5.— The telescope pointing for spectra of calibration stars taken during night of July 23, 2008 observing run. The observations used to fit the atmospheric model are shown as solid dots, and the solid lines trace the temporal order of the observations.

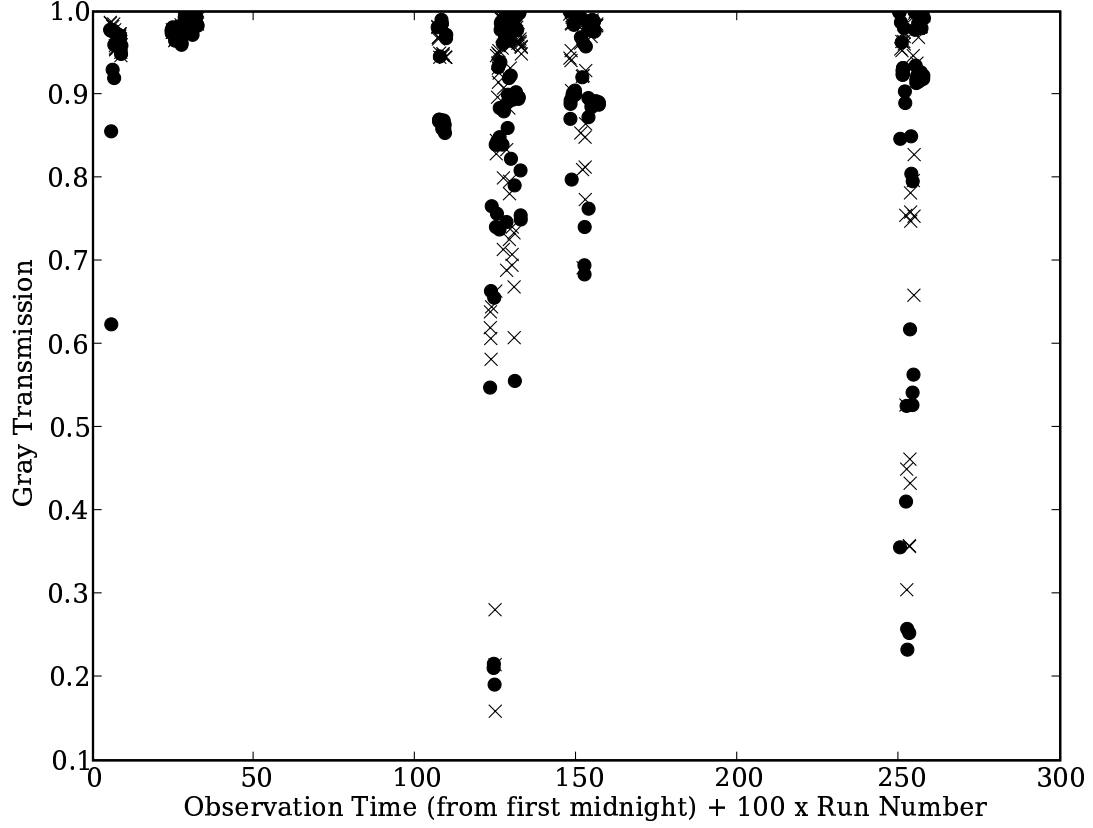


Fig. 6.— The coefficients T_{gray} from fits to spectra taken with the “red” set-up of the spectrograph. Calibration observations (•) and test observations (×) are shown separately. The horizontal axis is the running time in hours from UT midnight of the first night (00:00:00 UT November 2, 2007) plus 100 times the run number (0 for Nov 2007 and 2 for July 2008).

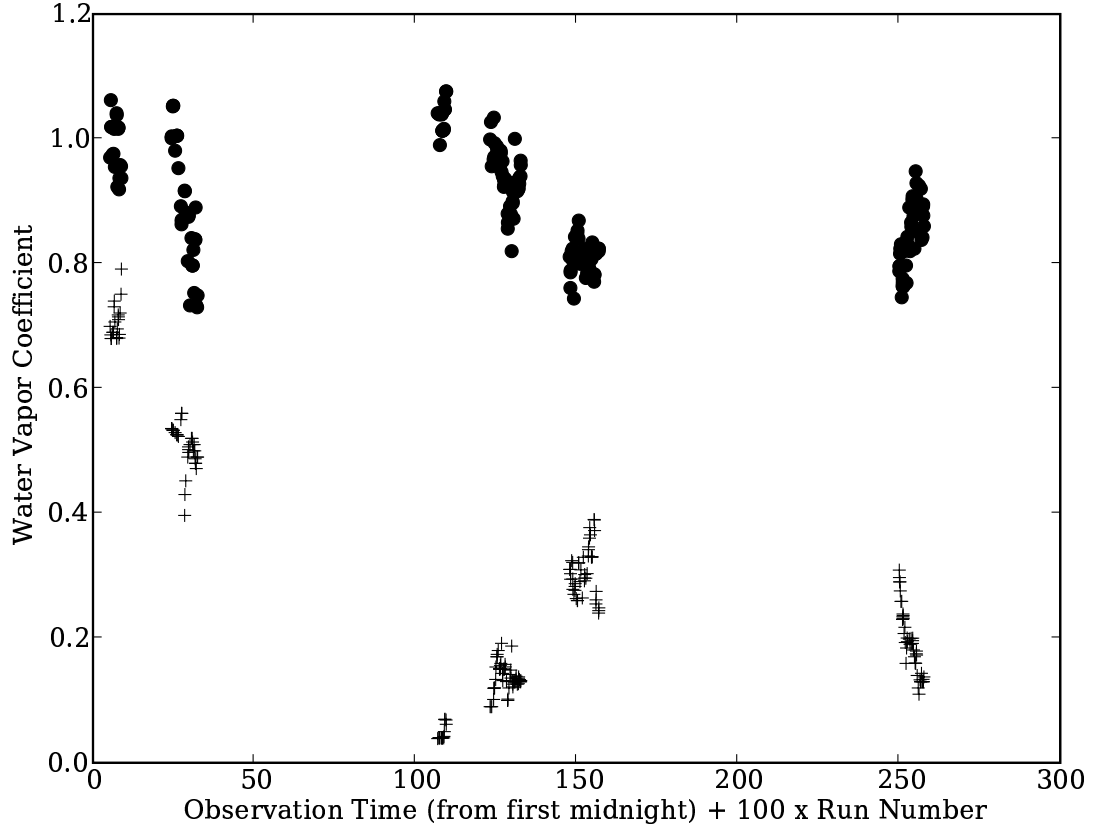


Fig. 7.— The coefficients C_{H_2O} (●) from fits to calibration spectra taken with the “red” set-up of the spectrograph. The horizontal axis is the same as in Figure 6. Also shown in this figure are readings of relative humidity (+) taken by the Tololo ground weather station. The vertical axis has different meanings for the two sets of points.

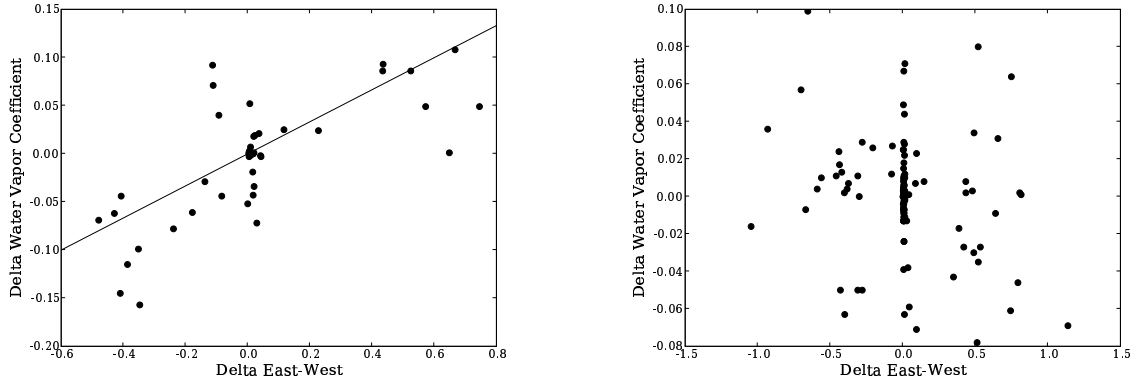


Fig. 8.— Spatial variation of water vapor measured as the change in the coefficient C_{H_2O} with change in the east-west pointing of the telescope. The plot on the left is for nights in November 2007 and that on the right for nights in April 2008. The data from November are described by a slope of 0.166 while the data from April are consistent with zero slope. Note that the vertical scales of the two plots differ.

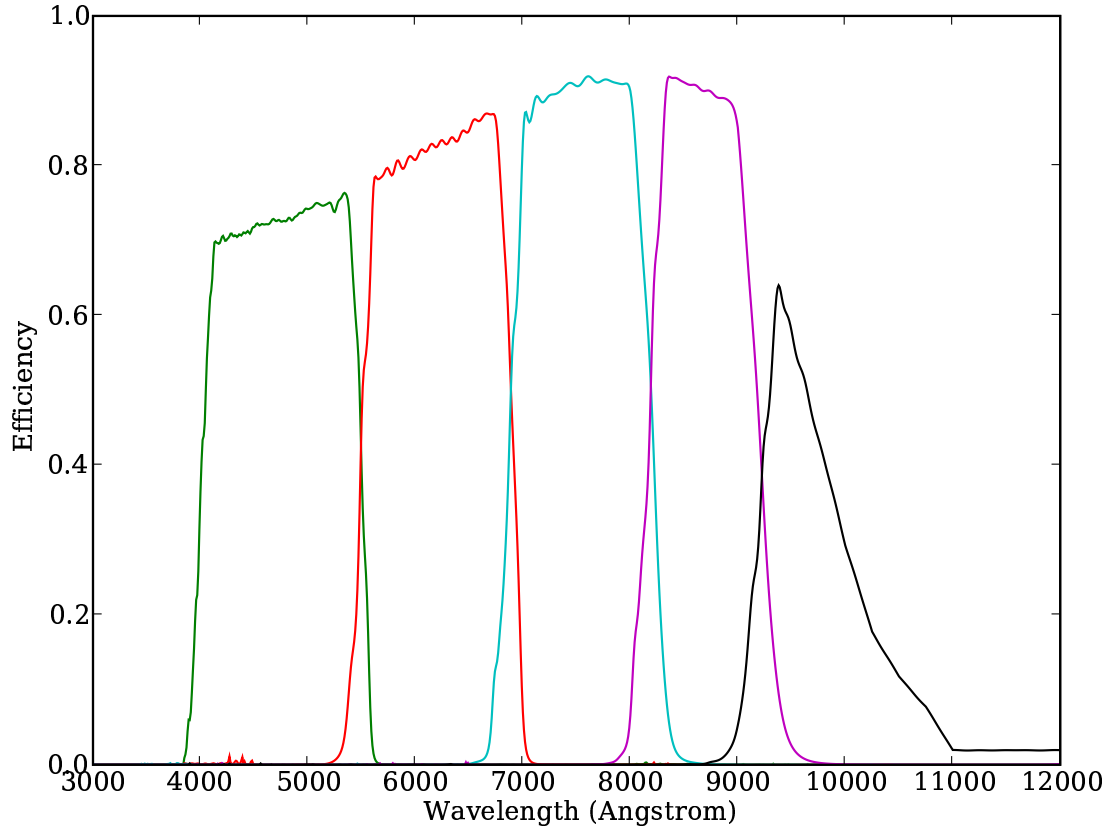


Fig. 9.— Instrumental throughput of synthetic *grizy* filters used in this study. The vertical axis is the overall normalized efficiency of the telescope, filter, and camera optics and sensors.

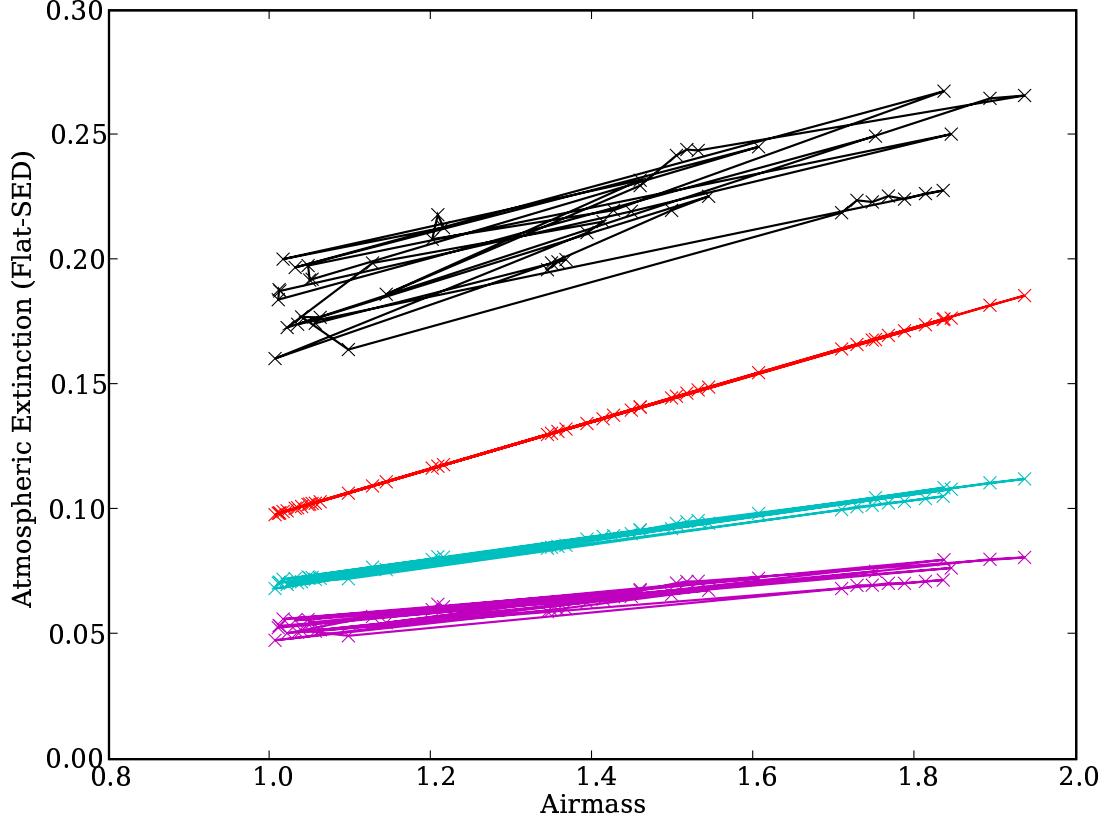


Fig. 10.— Example of non-gray atmospheric extinction (magnitudes) computed from model coefficients fitted to calibration observations for the night of July 23, 2008. The horizontal axis is the airmass of the observation computed from the telescope altitude. Extinction is computed for synthesized r (red), i (cyan), z (magenta), and y (black) bandpasses. The solid lines trace the temporal sequence of the observations used in the calibration.

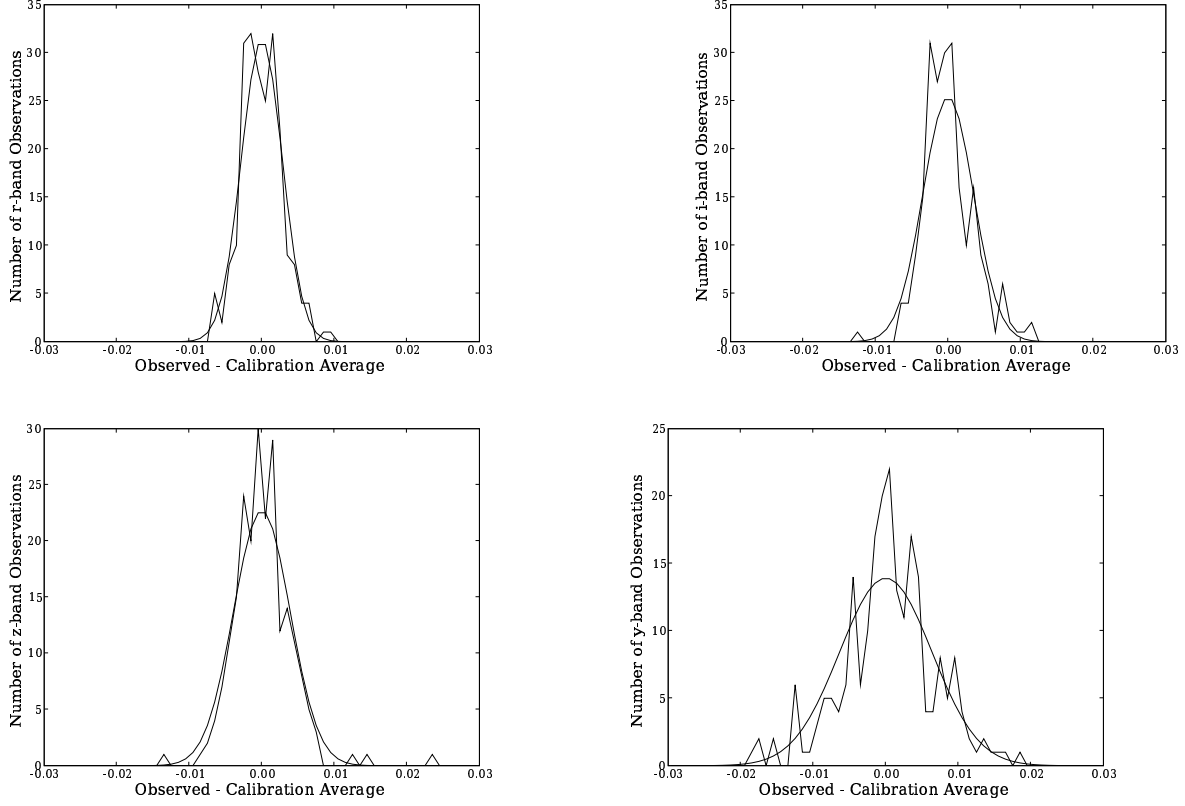


Fig. 11.— Dispersions of the fully-corrected (including “gray” corrections) top-of-the-atmosphere calibration magnitudes. The horizontal axis is the difference between magnitudes from individual observations of a star and the mean magnitude from all observations of the same star. Over and under flow counts would be accumulated in bins at the extreme ends of the horizontal range. (There are none in this data sample.) Values are shown for r (upper left), i (upper right), z (lower left), and y (lower left) bandpasses. The curves are Gaussian functions with σ equal to the rms of the offsets of individual observations from their corresponding mean.

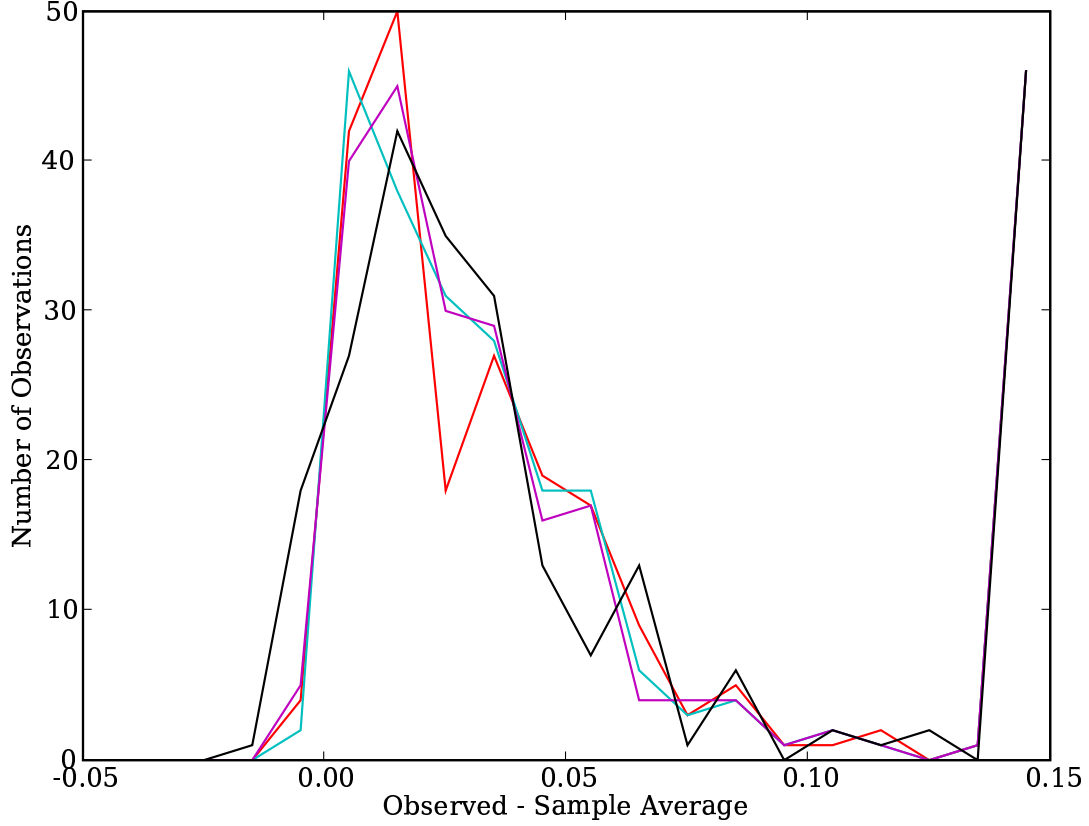


Fig. 12.— Offsets of blind observations when no “gray” correction is applied. The horizontal axis is the difference between magnitudes of individual observations and the mean of all observations of the same star. Over and under flow counts are accumulated in bins at the extreme ends of the horizontal range. Values are shown for r (red), i (cyan), z (magenta), and y (black) bandpasses.

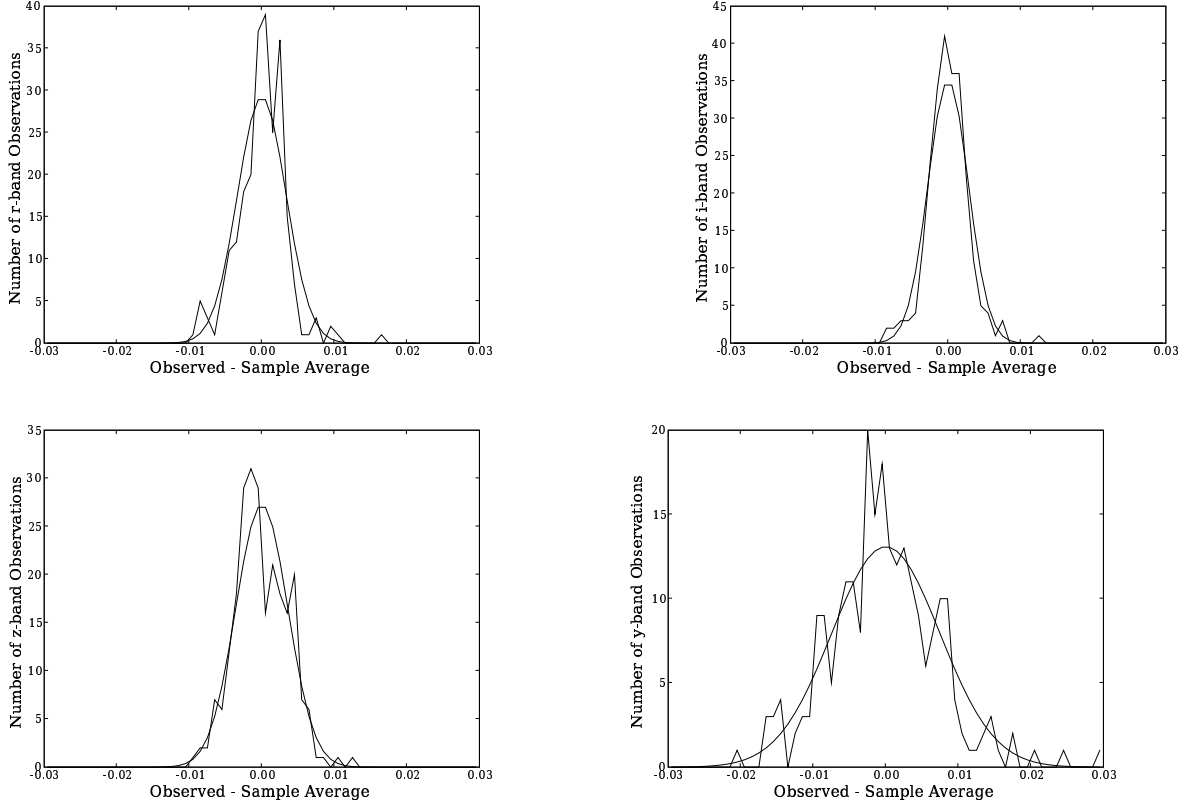


Fig. 13.— Offsets (dispersion) of blind observations after correction for “gray” extinction fitted to each observation. The horizontal axis is the same as that in Figure 12, but note the different scales. Values are shown for r (upper left), i (upper right), z (lower left), and y (lower right) bandpasses. The curves are Gaussian functions with σ equal to the rms of the offsets of individual observations from their corresponding mean.

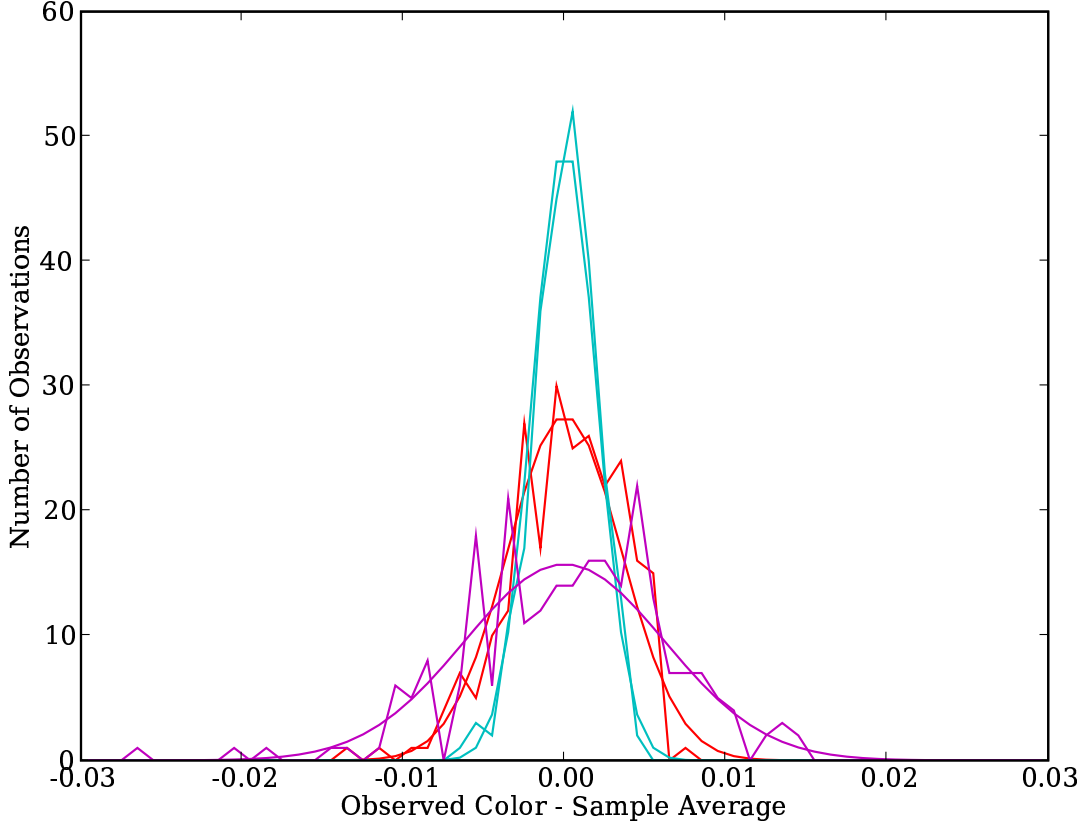


Fig. 14.— Offsets (dispersion) of colors computed from magnitudes of blind observations. The horizontal axis is the difference between colors of individual blind observations and the mean color of all observations of the same star. Over or under flow counts are accumulated in bins at the extreme ends of the horizontal range. Values are shown for $r - i$ (red), $i - z$ (cyan), and $z - y$ (magenta) colors. The curves are Gaussian functions with σ equal to the rms of the offsets of individual observations from their corresponding mean.